



City Research Online

City, University of London Institutional Repository

Citation: Sriratanavaree, S., Rahman, B. M., Leung, D. M. H., Kejalakshmy, N. & Grattan, K. T. V. (2014). Rigorous characterization of acoustic-optical interactions in silicon slot waveguides by full-vectorial finite element method. *Optics Express*, 22(8), pp. 9528-9537. doi: 10.1364/oe.22.009528

This is the unspecified version of the paper.

This version of the publication may differ from the final published version.

Permanent repository link: <https://openaccess.city.ac.uk/id/eprint/3611/>

Link to published version: <https://doi.org/10.1364/oe.22.009528>

Copyright: City Research Online aims to make research outputs of City, University of London available to a wider audience. Copyright and Moral Rights remain with the author(s) and/or copyright holders. URLs from City Research Online may be freely distributed and linked to.

Reuse: Copies of full items can be used for personal research or study, educational, or not-for-profit purposes without prior permission or charge. Provided that the authors, title and full bibliographic details are credited, a hyperlink and/or URL is given for the original metadata page and the content is not changed in any way.

City Research Online:

<http://openaccess.city.ac.uk/>

publications@city.ac.uk

Rigorous characterization of acoustic-optical interactions in silicon slot waveguides by full-vectorial finite element method

S. Sriratanavaree,* B. M. A. Rahman, D. M. H. Leung, N. Kejalakshmy and K. T. V. Grattan

School of Engineering and Mathematical Sciences, City University London, Northampton Sq., London, EC1V 0HB, UK

**suchara_b@hotmail.co.uk*

Abstract: For the first time detailed interactions between optical and acoustic modes in a silicon slot waveguide are presented. A new computer code has been developed by using a full-vectorial formulation to study the acoustic modes in optical waveguides. The results have shown that the acoustic modes in an optical slot waveguide are not purely longitudinal or transverse but fully hybrid in nature. The model allows the effects of Stimulated Brillouin Scattering and the associated frequency shift due to the interaction of these hybrid acoustic modes with the fully hybrid optical mode also to be presented.

©2014 Optical Society of America

OCIS codes: (000.4430) Numerical approximation and analysis; (290.5900) Scattering, stimulated Brillouin; (230.7370) Waveguides; (190.0190) Nonlinear optics; (190.2640) Stimulated scattering, modulation, etc.; (130.0130) Integrated optics; (130.2790) Guided waves.

References and links

1. K. Hotate and M. Tanaka, "Distributed fiber Brillouin strain sensing with 1-cm spatial resolution by correlation based continuous-wave technique," *IEEE Photon. Technol. Lett.* **14**(2), 179–181 (2002).
2. K. Y. Song, K. S. Abedin, K. Hotate, M. González Herráez, and L. Thévenaz, "Highly efficient Brillouin slow and fast light using As₂Se₃ chalcogenide fiber," *Opt. Express* **14**(13), 5860–5865 (2006).
3. V. R. Almeida, Q. Xu, C. A. Barrios, and M. Lipson, "Guiding and confining light in void nanostructure," *Opt. Lett.* **29**(11), 1209–1211 (2004).
4. D. M. H. Leung, N. Kejalakshmy, B. M. A. Rahman, and K. T. V. Grattan, "Rigorous numerical analysis and characterization of silicon vertical-slot nano-waveguide," *J. Nonlinear Opt. Phys.* **21**(01), 1250007 (2012).
5. S. Wang, J. Hu, H. Guo, and X. Zeng, "Optical Cherenkov radiation in an As₂S₃ slot waveguide with four zero-dispersion wavelengths," *Opt. Express* **21**(3), 3067–3072 (2013).
6. F. Dell'Olio and V. M. N. Passaro, "Optical sensing by optimized silicon slot waveguides," *Opt. Express* **15**(8), 4977–4993 (2007).
7. T. Baehr-Jones, B. Penkov, J. Huang, P. Sullivan, J. Davies, J. Takayesu, J. Luo, T.-D. Kim, L. Dalton, A. Jen, M. Hochberg, and A. Scherer, "Nonlinear polymer-clad silicon slot waveguide modulator with a half wave voltage of 0.25 V," *Appl. Phys. Lett.* **92**(16), 163303 (2008).
8. J. T. Robinson, K. Preston, O. Painter, and M. Lipson, "First-principle derivation of gain in high-index-contrast waveguides," *Opt. Express* **16**(21), 16659–16669 (2008).
9. R. M. Shelby, M. D. Levenson, and P. W. Bayer, "Guided acoustic-wave Brillouin scattering," *Phys. Rev. B Condens. Matter* **31**(8), 5244–5252 (1985).
10. J. E. McElhenny, R. K. Pattnaik, and J. Toulouse, "Dependence of frequency shift of depolarized guided acoustic wave Brillouin scattering in photonic crystal fibers," *J. Lightwave Technol.* **29**(2), 200–208 (2011).
11. K. J. Lee, H. C. Park, and B. Y. Kim, "Highly efficient all-fiber tunable polarization filter using torsional acoustic wave," *Opt. Express* **15**(19), 12362–12367 (2007).
12. W. Zou, Z. He, and K. Hotate, "Acoustic modal analysis and control in W-shaped triple-layer optical fibers with highly-germanium-doped core and F-doped inner cladding," *Opt. Express* **16**(14), 10006–10017 (2008).
13. Y. S. Mamdem, E. Burov, L. A. de Montmorillon, Y. Jaouën, G. Moreau, R. Gabet, and F. Taillade, "Importance of residual stresses in the Brillouin gain spectrum of single mode optical fibers," *Opt. Express* **20**(2), 1790–1797 (2012).

14. A. Safaai-Jazi and R. O. Claus, "Acoustic modes in optical fiberlike waveguides," *IEEE Trans. Ultrason. Ferroelectr. Freq. Control* **35**(5), 619–627 (1988).
 15. P. E. Lagasse, "Higher-order finite element analysis of topographic guides supporting elastic surface waves," *J. Acoust. Soc. Am.* **53**(4), 1116–1122 (1973).
 16. G. O. Stone, "Higher-order finite elements for inhomogeneous acoustic guiding structures," *IEEE Trans. Microw. Theory Tech.* **21**(8), 538–542 (1973).
 17. B. M. A. Rahman and J. B. Davies, "Finite element solution of integrated optical waveguides," *J. Lightwave Technol.* **2**(5), 682–688 (1984).
 18. D. M. H. Leung, N. Kejalakshmy, B. M. A. Rahman, and K. T. Grattan, "Rigorous modal analysis of silicon strip nanoscale waveguides," *Opt. Express* **18**(8), 8528–8539 (2010).
 19. A. B. Ruffin, M. J. Li, X. Chen, A. Kobayakov, and F. Annunziata, "Brillouin gain analysis for fibers with different refractive indices," *Opt. Lett.* **30**(23), 3123–3125 (2005).
-

1. Introduction

The field of *silicon photonics* allows both the exploitation of standard Complementary Metal-Oxide-Semiconductor (CMOS) fabrication techniques and integration of photonics with microelectronics allowing the development of a range of novel devices. Stimulated Brillouin Scattering (SBS) in optical waveguides is an important, but often undesirable nonlinear effect which arises from the coherent interactions between the optical and acoustic modes and limits power scaling in many photonic devices. However the effect can be exploited in strain or temperature sensing [1] and by controlling the SBS bandwidth [2] 'slow waves' can be generated to achieve tuneable pulse delays. Alternatively, waveguides can be designed to suppress SBS, for example for the transmission of high laser powers.

The slot waveguide [3, 4] is a unique structure in which light is guided in a low-index region due to the continuity of the normal component of the Electric Flux Density (\mathbf{D}) at the dielectric interfaces, which opens up new opportunities for sensor design [5, 6] where the slots can be filled with an active or functional material to create devices such as high-speed modulators [7], amplifiers [8] or nonlinear devices [5] by accessing higher field readily accessible in the slot region. The high index contrast also makes the optical modes are hybrid in nature, requiring a full-vectorial numerical method to characterize such structures. Guiding acoustic modes would also be possible if at least one of the velocities (the shear or longitudinal velocities) of the cladding exceeds that of the core. The particle displacement can be either longitudinal or transverse creating longitudinal, torsional, bending or flexural modes. Guided Acoustic Wave Brillouin Scattering (GAWBS), first studied in 1985 [9], where radial modes can be beneficial or detrimental [10] (as with SBS) but flexural and torsional acoustic modes have been exploited in the development of all-fiber acousto-optic tuneable filters [11]. Thus it is necessary to consider *all* the modes to characterize fully acousto-optic interactions.

Simple scalar formulations [12, 13] are often used to study longitudinal modes, or radial flexural modes [14] but are usually inadequate due to the complexity of the acoustic modes in such optical waveguides. A rigorous full-vectorial analysis method provides a more accurate characterization of such acoustic wave propagation and thus a simulation using the versatile Finite Element Method (FEM) has been developed to allow, for the first time, an analysis of acoustic modes and their interactions with the optical modes in slot optical waveguides.

2. Theory

The propagation of the acoustic wave generated due to an intense light beam passing through a slot waveguide linking to the periodic distortion of the waveguide along the axial and transverse directions-creates a periodic moving density grating, due to both material deformation and associated elasto-optic effects. This moving Bragg grating reflects the light which, as the acoustic wave is also travelling, is subject to 'down shifting' through the Doppler effect. Above the threshold pump power, which is much smaller than the Raman threshold power and in the mW range, the process becomes stimulated and the acoustic and

Stokes waves grow through mutual reinforcement. Modal solutions of acoustic modes in modern optical waveguides, which can be of arbitrary shape, with boundary conditions at both the material interfaces and also at the boundary, can make an analytical approach unsuitable. As a result, numerical approaches are preferred, particularly for optical waveguides of sub-acoustic wavelength dimensions. The FEM has been exploited previously to analyze vectorial acoustic modes but here this has been extended to general tensor and complex valued material parameters (to consider material loss if necessary), and for the first time interactions in silicon photonic structures are reported.

The propagation of an acoustic wave along the z direction may be associated with molecular displacement and for a time harmonic wave, the displacement vectors, \mathbf{U}_i , can be written in the following form [15]:

$$\mathbf{U}_i = \mathbf{u}(u_x, u_y, ju_z) \exp\{j(\omega_a t - k_a z)\} \quad (1)$$

where the angular acoustic frequency, ω_a , reveals the time dependence; the propagation constant, k_a identifies the axial dependence of the acoustic wave and u_x , u_y and u_z are the particle displacement vectors along the x , y and z directions respectively. The deformation in an acoustically vibrating body can be described through the strain field, \mathbf{S} , which relates to the partial derivative of particle displacements and is given by:

$$\mathbf{S} = \nabla \mathbf{u} \quad (2)$$

The elastic restoring forces can be defined in terms of the stress field, \mathbf{T} and the inertial and elastic restoring forces in a freely vibrating medium are related through Newton's equation of motion, as shown below:

$$\nabla \cdot \mathbf{T} = \rho \frac{\partial^2 \mathbf{u}}{\partial t^2} \quad (3)$$

where ρ is the density of the material. Hooke's Law states that the strain and stress are linearly proportional to each other and thus:

$$T_{ij} = c_{ijkl} S_{kl}; \quad i, j, k, l = x, y, z \quad (4)$$

where the microscopic spring constants, c_{ijkl} , are termed the elastic stiffness constants. The constitutive relation given by the compliance and stiffness tensors can be denoted in matrix form by:

$$[T] = [c][S] \quad (5)$$

in which c_{ijkl} is a fourth order tensor and the stiffness constant tensor $[c]$ is 9×9 but as it obeys the symmetry condition, it can be represented by using two suffix notations, thus reducing to a 6×6 matrix. In the simplest case of an isotropic, homogeneous and bulk material, this can be represented by two terms only of the Lamé constants relating the shear and longitudinal velocities. Thus in this work, the waveguide cross-section region, Ω , is sub-divided into an assemblage of triangular elements where the material displacement and spatial derivatives within each element can be defined in terms of the nodal values of these triangles.

Classically, in the FEM [15, 16] for a solid structure, the displacement field, \mathbf{u} , can be written using the interpolation shape function, $[N]$, and of the vector of the nodal values of the displacement field \mathbf{u} where:

$$\mathbf{u} = \begin{Bmatrix} u_x \\ u_y \\ u_z \end{Bmatrix} = \begin{bmatrix} N_1 & 0 & 0 & N_2 & 0 & 0 & N_3 & 0 & 0 \\ 0 & N_1 & 0 & 0 & N_2 & 0 & 0 & N_3 & 0 \\ 0 & 0 & N_1 & 0 & 0 & N_2 & 0 & 0 & N_3 \end{bmatrix} \begin{bmatrix} u_x^1 \\ u_y^1 \\ u_z^1 \\ u_x^2 \\ u_y^2 \\ u_z^2 \\ u_x^3 \\ u_y^3 \\ u_z^3 \end{bmatrix} \quad (6)$$

By representing $[S]$ in terms of the spatial variations of the displacement vectors, \mathbf{u} , as shown by Eq. (2), and relating the stress and strain via Eq. (5), the time harmonic acoustic wave problem can be reduced to a general eigenvalue equation:

$$([A] - \omega_a^2 [B])\mathbf{U} = F \quad (7)$$

where $[A]$ is the stiffness matrix, related to strain energy and $[B]$ is the mass matrix related to the kinetic energy. In this case, if necessary, the full $[c]$ matrix or its reduced form can be used. These matrices are generated for a given acoustic propagation constant, k_a . The column vectors, F , contain the nodal values of the applied forces, which in this case are taken to be equal to zero. Solving this generalized eigenvalue equation of the system yields the eigenvalue as ω_a^2 , where ω_a is the angular acoustic frequency and the eigenvector \mathbf{U} , the displacement vector.

The FEM approach is used to analyze the light guidance and this is based on the vector- \mathbf{H} -Field formulation, to provide one of the most accurate and numerically efficient approaches to obtaining the modal field profiles and propagation constants of the fundamental and higher-order quasi-TE and quasi-TM modes. The full-vectorial formulation is based on the minimization of the full \mathbf{H} -field energy functional [17],

$$\omega_o^2 = \frac{\int [(\nabla \times \mathbf{H})^* \cdot \hat{\epsilon}^{-1} (\nabla \times \mathbf{H}) + p (\nabla \cdot \mathbf{H})^* (\nabla \cdot \mathbf{H})] dx dy}{\int \mathbf{H}^* \cdot \hat{\mu} \mathbf{H} dx dy} \quad (8)$$

where \mathbf{H} is the full-vectorial magnetic field, * denotes a complex conjugate and transpose, ω_o^2 is the eigenvalue where ω_o is the optical angular frequency of the wave, p is a weighting factor for the penalty term and $\hat{\epsilon}$ and $\hat{\mu}$ are the permittivity and permeability, respectively and these material parameters can be arbitrarily tensor.

The two-dimensional cross-section of the waveguide is discretized by using many first order triangular elements and all three components of the magnetic fields required for the optical model and the displacement vectors for the acoustic model may be represented by piece-wise polynomials within the elements. The same mesh discretization is used for both the models, so that their interactions can be accurately calculated by integrating the functional over each element.

3. Results

The unique feature of a slot waveguide (SW) is that light is guided in a low index region, which may also be air. However, to create a functional device, the slot region can also be filled with nonlinear or active materials but with the condition that this material should have a lower refractive index.

Sound will also be guided in this slot region when filled with silica (SiO_2), as it has a higher acoustic index than the surrounding silicon (Si) layer, creating sound-light interactions in the slot waveguide. Frequently a low-index SiO_2 buffer layer is used to isolate the optical mode from the high index Si substrate, but this will not isolate acoustic wave. To achieve both optical and acoustic modes isolation, a low index (both optical and acoustic) silica nitride (Si_3N_4) layer is envisaged. A typical air-clad SiO_2 -filled slot waveguide structure of width, $W_s = 150$ nm and height, $H = 220$ nm (with a Si core width $W = 300$ nm on either side and Si_3N_4 buffer layer at the bottom of the slot to prevent the leakage of the slot mode to the bottom of the layer, where $B = 1$ μm) is considered to study these various acoustic modes, as shown as an inset in Fig. 1. The longitudinal acoustic velocities in SiO_2 , Si and Si_3N_4 are taken as 5736, 8433 and 11611 m/s and those of the acoustic shear velocities are assumed to be 3625, 5845 and 5956 m/s, respectively.

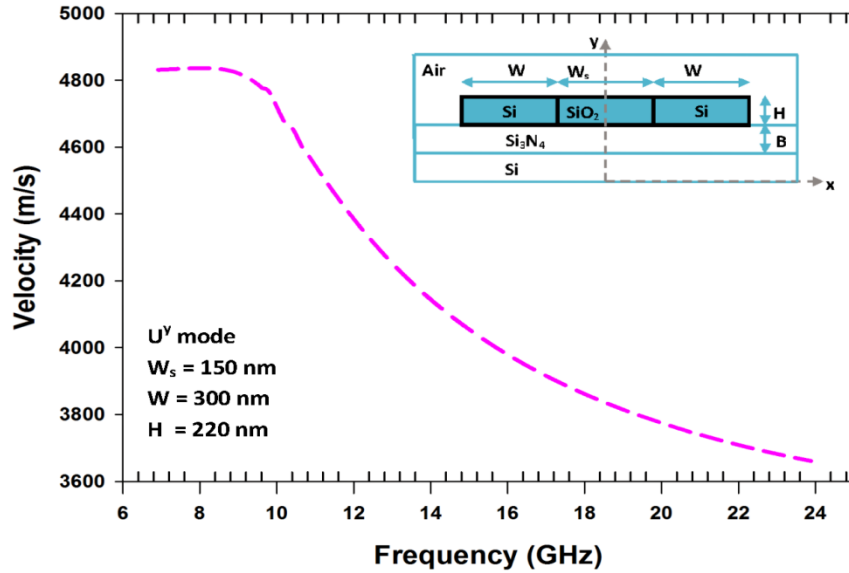


Fig. 1. Variation of the phase velocity of the U^y acoustic mode with the frequency for a vertical slot waveguide.

The variation of the acoustic wave velocity with the operating frequency for the fundamental U^y mode is also shown in Fig. 1. A notation similar as used for the optical modes is used here where a mode is identified by its dominant displacement vector, where for this U^y mode, its displacement in y -direction (U_y) is a maximum. As the operating frequency is reduced, the acoustic wave velocity asymptotically approaches its modal cutoff towards a velocity which is related to the slab acoustic mode of a 220 nm thick Si layer. Similarly as the frequency is increased, the mode asymptotically reaches a value for a very well confined mode in the SiO_2 slot region. For this range, the acoustic velocity, which is equal to the ratio ω_a/k_a , also reduces monotonically from 4838 m/s to 3456 m/s as the frequency increases from 6 GHz to 24 GHz.

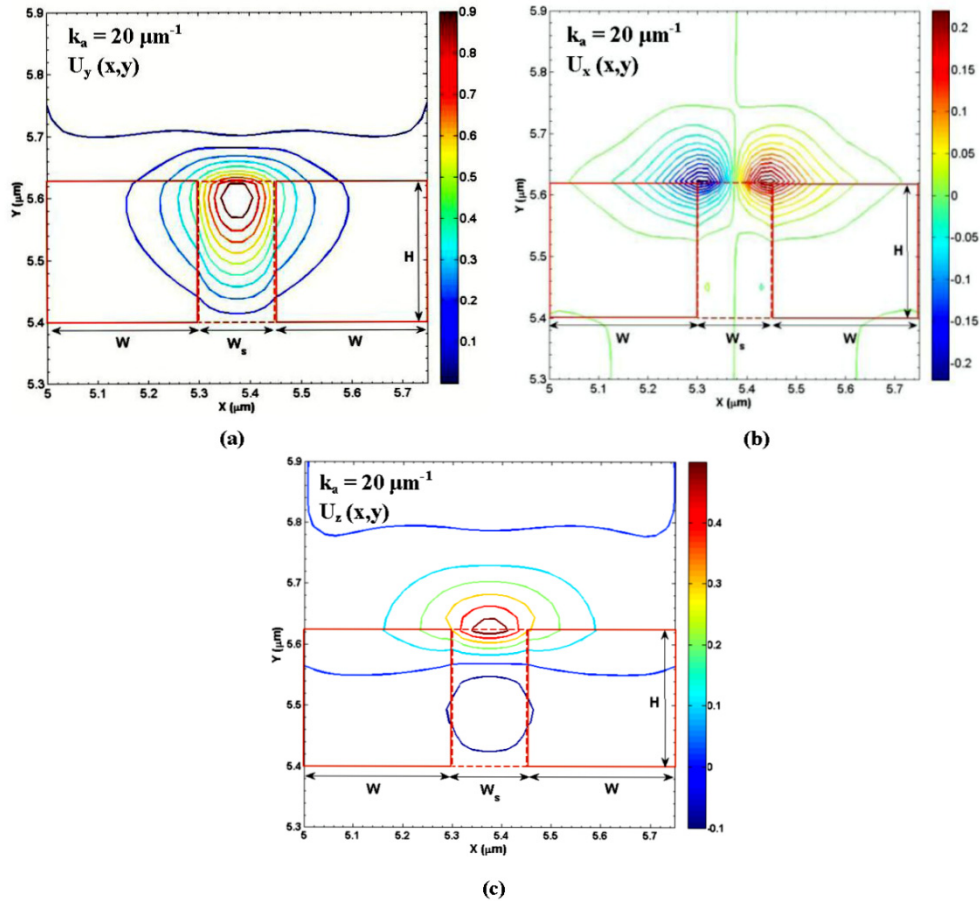


Fig. 2. The displacement vector plots of the U^Y mode in a slot waveguide with (a) U_y (b) U_x and (c) U_z displacement vector profiles at $k_a = 20 \mu\text{m}^{-1}$.

The full-vectorial eigenvector profile of this U^Y mode is shown in Fig. 2 for a propagation constant, k_a , equal to $20 \mu\text{m}^{-1}$, with the positions of the Si waveguides and the slot region shown by red solid and dashed lines respectively. For this mode, the U_y displacement vector is shown in Fig. 2(a), normalized to unity. The U_y profile is symmetric along the horizontal direction with its peak value located inside the slot region but not symmetric in the vertical direction, as the material properties of the upper and lower sides were different. The non-dominant U_x profile of this U^Y mode is shown in Fig. 2(b) where this vector is anti-symmetric with a higher order spatial variation in the lateral direction, in a way similar to the non-dominant field of a Si waveguide [18]. Its maximum magnitude is about 20% of the maximum value of the dominant U_y displacement vector, which lies along the upper interface where acoustic index contrast was higher. Figure 2(c) shows another non-dominant $U_z(x,y)$ vector profile with a higher order spatial variation, but this time in the vertical direction which is also highly non-symmetrical but with a symmetric profile along the horizontal direction. Its highest value is about 50% of that of the dominant U_y displacement vector and is located at the upper slot interface where material contrast was higher. For this U^Y mode, as the U_y displacement vector was dominant, it also contains other displacement vectors including a longitudinal U_z component. Figure 1 has shown that as the operating frequency (or k_a) reduced as the U^Y mode approached its cutoff and when the propagation constant increases, the displacement vectors had smaller spatial spread. The full-mode-width of the U_y

vector along the horizontal direction (where the field decays to $1/e$ of its maximum) is 180 nm and 132 nm respectively for propagation constants $k_a = 20$ and $40 \mu\text{m}^{-1}$, respectively. Figure 2 clearly demonstrates their symmetry along the vertical axis, as the structure had the one-fold symmetry, but not in the vertical direction.

To study the effect of this non-symmetry, the variations of the dominant displacement vector U_y of the U^y mode along the vertical direction is shown in Fig. 3, for two different k_a values. The U_y profile is not symmetric but tilted and instead of the full-mode-width, only half-mode-widths along both lower and upper directions are calculated (separately) to be 133 nm and 20 nm respectively for $k_a = 20 \mu\text{m}^{-1}$ where its peak value is closer to the upper interface where the material index difference was greater. A small negative peak can also be observed in the upper cladding layer, where similar negative peaks for all acoustic waveguide are seen when they have a strong index contrast, a feature missing for an acoustic waveguide with a small acoustic index contrast. For a higher propagation constant $k_a = 40 \mu\text{m}^{-1}$, shown in the figure by a red dashed line, the mode profile is narrower and the negative peak is sharper with a higher secondary peak value. When k_a is increased to $40 \mu\text{m}^{-1}$, these half-mode-widths in the lower and upper directions reduce to 94 nm and 10 nm, respectively, these being much smaller values than are seen for $k_a = 20 \mu\text{m}^{-1}$.

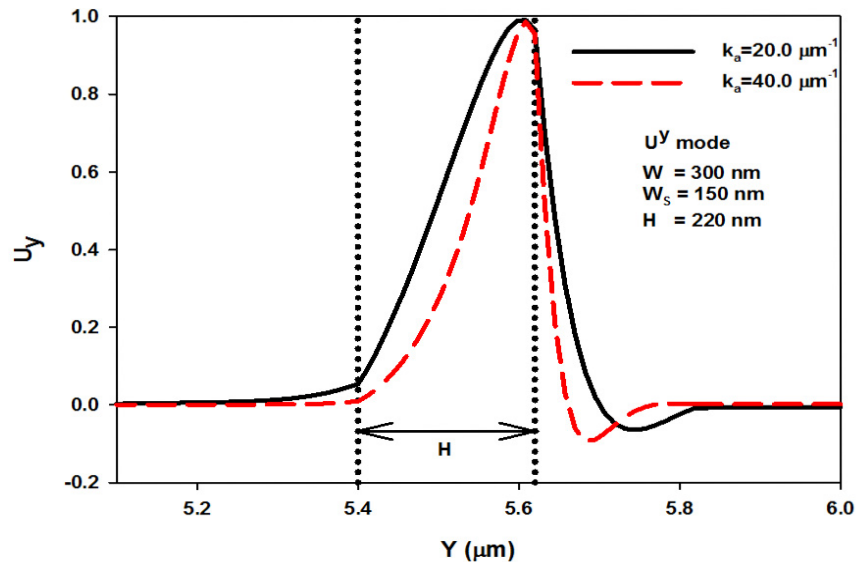


Fig. 3. Variations of displacement vector U_y of the U^y mode along the y -axis for $k_a = 20.0 \mu\text{m}^{-1}$ and $k_a = 40.0 \mu\text{m}^{-1}$.

As the propagation constant increases, the non-dominant displacement vector profiles also shrink but their magnitudes increase, signifying that as propagation constant (or the frequency) increases, the modes are more confined but also more hybrid in nature. The maximum value of the longitudinal displacement vector, U_z , is comparable to the maximum U_y value, and being large for this U^y mode, it is not purely transverse mode but a highly hybrid creating a complex interaction with the optical modes. When the slot width was reduced, the U^y mode approaches its cutoff value at a lower acoustic frequency but with a slightly higher acoustic velocity. By contrast, when the slot height is increased, its cutoff value is reached at a lower acoustic frequency, but approaches the same acoustic velocity.

Optical solutions of the Si slot waveguides were obtained by using a full-vectorial \mathbf{H} -field formulation [17] allowing the interactions of the acoustic and optical modes to be studied. The variation of the effective index (n_{eff}) for a quasi-TE mode with the slot width, W_s , is

shown in Fig. 4. Although both quasi-TE and quasi-TM modes can exist for this structure, only the quasi-TE mode will have a sufficiently high power density in the slot region due to the enhancement of D_x in the slot region and thus this mode is considered. It can be observed that as the W_s reduces, the value of n_{eff} increases. This slot mode can also be described as the even supermode of the coupled Si waveguides, where n_{eff} increases as the separation between the guides (similar to W_s) reduces. However, as the constituent Si waveguides are rather narrow, they cannot support a mode on their own, so an odd supermode for this structure does not exist. The variation of the effective mode area (A_{eff}) is also shown in this figure by a dashed line. The optical slot-mode only exists when W_s is not wide – the slot confines light better in the low index region.

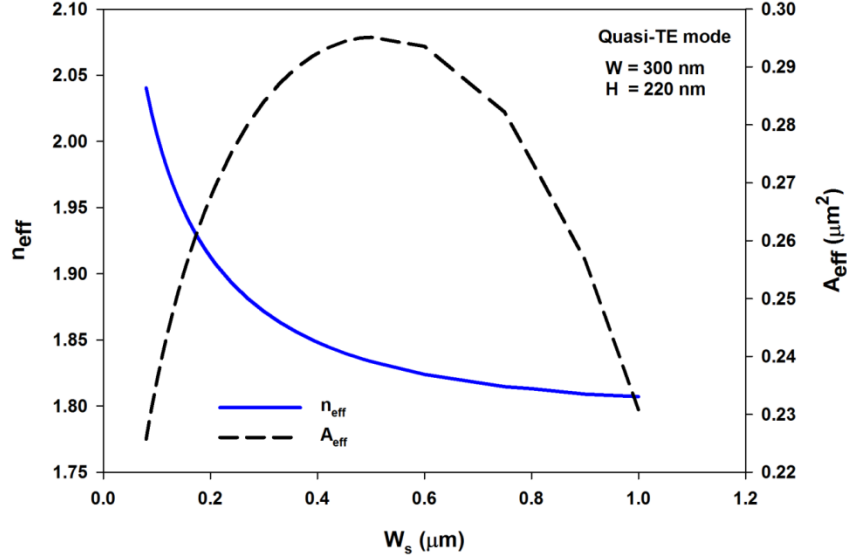


Fig. 4. Variations of the effective index, n_{eff} , and effective area, A_{eff} , with the slot width, W_s .

Periodic material displacement arising from the acoustic mode introduces density variations which generate a Bragg Grating giving rise to changes in the refractive indices. Additionally, these periodic stress variations also introduce refractive index variations (which are anisotropic) due to the elasto-optic effects and the optical intensity variation will also create an acoustic wave via electro-striction effects. For the U^y mode, its U_y profile was very similar in shape to the modal field profile of the fundamental quasi-TE optical mode, so their overlap is expected to be significant. Due to the time dependent optical density variation, the optical and sound waves interact with each other and can exchange energy if the phase matching condition is satisfied. Subsequently, the SBS frequency shift, f_B , can be calculated using this phase matching condition:

$$f_B = 2 n_{\text{eff}} V_a / \lambda_o \quad (9)$$

where n_{eff} is the effective index of the optical mode, V_a is the acoustic velocity, λ_o is optical wavelength and

$$k_a = 2 \beta_o \quad (10)$$

where k_a is the acoustic wavenumber and β_o is the optical propagation constant. For a given structure, the propagation constant of the interacting optical mode, in this case the quasi-TE mode, i.e. β_o is calculated. Subsequently, using Eq. (10), the matched propagation constant, k_{as} , of the acoustic mode can be obtained, following which the phase velocity (V_a) of the

interacting acoustic mode (in this case U^y mode) may be calculated for this k_a value. Finally the SBS frequency shift, f_B is determined by using Eq. (9).

Figure 5 shows the SBS frequency shift that is predicted for the fundamental optical mode, for different waveguide slot widths (W_s), operating at $\lambda = 1.55 \mu\text{m}$, through the interaction of the U^y mode. For this structure, as the slot width is reduced, its optical effective index increases, in turn increasing both the optical propagation constant (β_o) and the phase matched acoustic propagation constant (k_a). The resultant acoustic modal velocity (V_a) was then calculated for this acoustic propagation constant (k_a), as was the SBS frequency shift (f_B), which increases as the slot width is reduced.

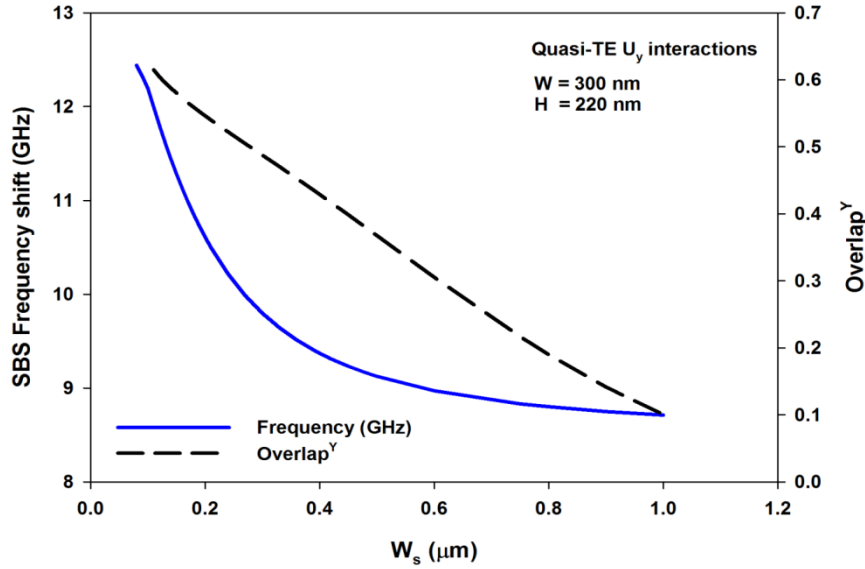


Fig. 5. Variations of the SBS frequency shift and modal overlap with the slot width, W_s .

A dimensionless acousto-optic modal overlap parameter is adopted in this work, as is often used in the literature [19], rather than the acousto-optic effective area [2]. The overlap between the dominant H_y field of the quasi-TE mode with the dominant displacement vector U_y of the transverse acoustic mode was also calculated and shown in Fig. 5. The overlap with the U_y vector increases almost linearly as the slot-width is reduced, as for this structure both the optical and acoustic modes become more confined in the narrow slot region. As this mode was fully hybrid, there may also be considerable overlap with the longitudinal displacement vector U_z and the H_y field of the quasi-TE mode. The U_z profiles were non-symmetric with positive and negative peaks along the vertical direction, but since these peaks were not equal, there was a reasonable overlap of this displacement vector with the optical field. This parameter was calculated for different slot waveguide dimensions where this value increases progressively as the slot width is reduced and reaches its maximum value of 0.18, when $W_s = 110 \text{ nm}$, and then rapidly reduces. The overlap of the optical field with the U_x vector was very small as this profile was anti-symmetric along the horizontal direction. As the slot height was increased its effective index increased, which in turn increases the SBS frequency shift. However, the overlap between the optical and acoustic waves reduces as the slot height increases. For this slot-waveguide as the Si core width, W rises, the effective index of the optical mode increases, which also increases the phase matched acoustic propagation constant (k_a) and the SBS frequency shift. In this case, the acousto-optical overlap integral also reduces as the waveguide width W is increased but only modestly.

4. Conclusion

For the first time, a simulation of the interaction of optical and acoustic modes employing full-vectorial approaches for both the optical and acoustic models was presented where identical mesh discretization has been used for both models and the interactions were calculated rigorously without interpolating the field variables. This offers a significant advance on work reported previously in which these important optical-acoustic interactions were studied, but often the vector natures of the modes were ignored and only approximate scalar formulations used. For sub-wavelength optical and acoustic waveguides, both the optical and acoustic modes are fully hybrid in nature and the work has shown that this requires rigorous full-vectorial approaches to determine the complex acousto-optical interactions. The acoustic wave not only changes refractive index to form moving gratings, but also the periodic stress variation will change the refractive index, due to elasto-optic effects which are fully anisotropic in nature. In this work, the SBS gain has not been shown. This not only depends on the SBS frequency shift and the acousto-optic modal overlap, which have been shown in Fig. 5, but also on the electro-striction tensors and acoustic modal loss values. For high optical power delivery, the SBS threshold power can be increased by reducing the acousto-optical modal overlap, but on the other hand for efficient distributed sensors this threshold power can be reduced, which depends on the SBS gain and optical loss coefficient. The versatile finite element approach developed here has thus demonstrated its effectiveness to study such interactions between fully vectorial acoustic and optical modes in practical waveguides and devices.